nature medicine

Article

https://doi.org/10.1038/s41591-023-02584-1

A spinal cord neuroprosthesis for locomotor deficits due to Parkinson's disease

In the format provided by the authors and unedited

SUPPLEMENTARY INFORMATION

DESIGN AND FABRICATION OF THE NHP EPIDURAL SPINAL ARRAYS

Spatial distribution of leg motor neuron pools

In order to identify which dorsal roots to target using the epidural spinal arrays, we used a previously generated library of the spatial distributions of motor neuron pools of lower limb muscles in macaque monkey[1,2]. Briefly, the library was assembled using retrograde tracing method in seven monkeys. The monkeys received injections of Fastblue (4 % in sterile saline, 1000 µl per muscle) or Fluoro-Ruby (10 % in sterile saline, 1000 µl per muscle) in up to two distinct muscles of the left and right legs, allowing tracing up to four muscles per monkey. The following muscles recorded during locomotion were traced: gluteus medius, iliopsoas, rectus femoris, semitendinosus, gastrocnemius medialis, tibialis anterior, extensor digitorum longus, and flexor hallucis longus. The locations of the retrogradely traced motor neurons were reconstructed in 3D from serial sections of the spinal cord using Neurolucida. The reconstruction from all the animals are merged into a unified digital library using the morphology of the spinal segments as a landmark.

Anatomy of the spine

To precisely determine the dimensions of the arrays that fit within the epidural spinal space, we leveraged the previously performed reconstruction of the macaque spine[1,2]. Briefly, the three-dimensional reconstruction of vertebra was conducted using the micro-computed-tomography scanner Skyscan 1076 (Bruker µCT). The 3D shape of vertebrae was derived from these scans using NRecon and GPURecon Server (Bruker µCT). The spinal cords of several monkeys were imaged post-mortem. Segmentation and 3D models were constructed with Amira® (FEI Vizualisation Sciences Group). The spinal cord and vertebra reconstructions were co-registered into a unified 3D model. Measurements of relationships between vertebra and spinal segment morphologies were performed on fresh tissue taken from cadavers. For each monkey, the spinal segments were identified based on the innervation of the dorsal roots. The centre of the segment was defined as the entry point of the rootlets. After measuring the length of vertebra, and the relationships between vertebra and spinal segments, the entire spinal cord was extracted, and the roots moved perpendicular to the spinal cord to clearly visualize the segments. The location and length of each segment was then calculated.

Reconstruction of spinal segments and dorsal root trajectories

We relied on the previously performed reconstruction of dorsal root trajectories[1,2]. Briefly, the spinal cords of three monkeys were dissected, fixated overnight, and transferred to 30% phosphate buffered sucrose for cryoprotection. The dura mater was opened along the rostrocaudal axis, and gently moved on the side. For each spinal segment, the dorsal root ganglions were identified. The corresponding root was retracted cranially and laterally. The entire length of the root was painted, from the cut extremity to the entrance into the spinal segment. All the painted roots from S1 to L1 were repositioned to their original location along spinal segments, and the dura mater was sutured. The spinal cord was then frozen and cut into 80 µm thick slices using a cryostat (Leica Instruments). Reconstructions were conducted using every 4 sections, corresponding to intervals of 320 µm. The slides were assembled into the Neurolucida image analysis software (MBF Bioscience) to reconstruct the color-coded dorsal roots trajectories and lumbosacral segments in 3D.

Using model of the spinal cord and vertebral morphology for implant design

All the 3D reconstructions derived from micro-computed-tomography scans and anatomical experiments were merged to generate a global model including the bony structure of the vertebrae, the shape of spinal segments, the trajectory of each dorsal root and the anatomical locations of motor neuron columns. We leveraged this model to design epidural spinal arrays that positioned the electrodes above the L2-L7 spinal dorsal roots. In order to fit the electrode contacts and the tracts in the dorsal space between the vertebra and the spinal cord, we designed two implants: an 8-electode "rostral" electrode array targeting left and right L2, L3 and L4 roots; and another 8-electode "caudal" electrode array targeting the L5, L6 and L7 roots. We designed each implant to access the roots on their way from the entry between the vertebra to their entry into the spinal cord.

Fabrication of NHP epidural spinal arrays using the e-dura technology

We developed a manufacturing procedure that uses the e-dura technology[3] to fabricate the NHP epidural spinal arrays. The manufacturing process involved five stages **(Extended Data Fig. 3a):**

1. Substrate

We use 4" silicon wafers as a substrate for the implants. We then spin-coat a polystyrene sulfonic acid layer on the carrier to provide a water-release layer for the substrate stack. We then cast a polydimethylsiloxane (PDMS) layer on the substrate to a thickness of approximately 500 µm. We then manually laminate a laser-machined, 50 µm thick polyimide mask on the PDMS surface, and mount the carriers in a thermal evaporation chamber. We thermally evaporate a stack of chromium and gold on the carriers through the polyimide masks at a thickness of 5 nm (Cr) and 55 nm (Au). The chromium acts as adhesion promoter for the gold interconnect on PDMS. We finally peel the polyimide shadow mask off the surface to reveal the interconnect design patterned in the metal stack.

2. Passivation

We cast a 3 mm thick PDMS handling layer in a Petri dish. Once cured, we expose the top surface to an oxygen plasma. We then apply a vapour-phase 1H,1H,2H,2H-perfluorooctyltriethoxysilane (Sigma-Aldrich) layer in a vacuum chamber. This inhibits the adhesion of the silicone to subsequent PDMS layers deposited on the surface. We spin-coat and cure two subsequent 20 µm thick PDMS layers on the thick PDMS, separated by the same adhesion inhibiting layer. We then cut this triple PDMS stack (3 mm, 20 µm, 20 µm in cross section) with a blade and mount it on a glass slide. We then use a mechanical catheter puncher to make holes through the two thin PDMS layers and into the thick handling layer, in order to machine the passivation stack with through-vias. Each via is created by punching a series of 4 round holes of 690 µm diameter with 400 µm centre-to-centre spacing.

3. Assembly

We expose the top surfaces of the substrate and triple stack encapsulation to oxygen plasma, and then mount them on an alignment rack with the two treated surfaces facing one another. We align the vias machined in the encapsulation with the interconnect patterned on the substrate. We then put the two parts into contact in order to form a covalent bond between the silicone layers. Once bonded, we peel the thick PDMS handling layer off the substrate, leaving the interconnect encapsulated by two 20 µm thick PDMS layers with openings corresponding to the position of the electrodes.

4. Electroactive coating

We prepare the electroactive coating as a composite material obtained by dispersing microscale platinum particles (Goodfellow PT006021, 3.5 µm maximum particle size) within a PDMS matrix. This creates a

conductive paste that offers a balance between the charge injection properties of platinum and the mechanical properties of PDMS. We apply this composite paste on the encapsulation through the screen print PDMS layer to fill the openings, which creates an electrical contact with the interconnect. We then peel the screen print layer off to remove the excess coating and define the active stimulation sites.

5. Packaging

We use a blade to manually cut the assembled implant to the desired shape while still on wafer. We thread the electrical wires in a PDMS guiding piece through holes that are machined at the same pitch as the gold tracks on the substrate. We then align this soft connector onto the interconnect with wires close to the ends of the gold tracks. To make the individual electrical connections between the wires and the gold tracks, we pressure-dispense conductive Ag paste (Epotek H27D). Once all electrical connections are made, we apply a bolus of room temperature vulcanization sealant (one component silicone sealant 734, Dow Corning) over the connector to secure mechanically the assembly. After the sealant is cured, we release the implant from the silicon carrier by dissolving the PSS layer under the PDMS substrate with DI water.

Throughout the manufacturing process, we prepare all silicone layers by mixing PDMS (Sylgard 184, Dow Corning) using a weight ratio of 10:1 between pre-polymer and cross-linker. The deposited layers are cured for a minimum of 3 hours in temperature controlled oven set to 80°C.

WIRELESS CONTROL OF SPINAL CORD STIMULATION

Implantable pulse generator

The epidural spinal arrays were interfaced with an Activa RC implantable pulse generator (Medtronic, USA) commonly used for deep brain stimulation therapies. Activa RC supports the delivery of monopolar, constant-current or constant-voltage stimulation protocols using the case of the generator as the anode. The Activa RC firmware supports the definition of pre-defined stimulation sequences. Each sequence is composed of one or more stimulation protocols, each characterized by (i) stimulation channel (mapped to one of 16 electrodes of the epidural spinal arrays), (ii) stimulation frequency, (iii) stimulation pulse width, (iv) stimulation duration, and (v) stimulation amplitude. The stimulation protocols can overlap each other. Activa RC enables wireless upload of stimulation sequences and the ability to initiate and stop each of those sequences. Reception of a new command immediately interrupts the execution of a previous sequence.

Wireless communication with the implanted pulse generator

We used a previously developed communication chain to wirelessly communicate with the implanted Activa RC pulse generator[2]. Briefly, our real-time analysis software running on the control computer elicited a stimulation sequence trigger command and sent it to a Neural Research Programmer software application (Medtronic, USA) running on the same computer. The Neural Research Programmer wirelessly transmitted the command by a Bluetooth link to a Bluetooth-to-infrared module placed in the jackets worn by the monkeys (ACTiSYS Inc.). The Bluetooth-to-infrared module relayed the command to the Patient's Programmer device (Medtronic, USA) in the jackets, which then transferred the command to the implanted Activa RC using a telemetry antenna placed on the monkeys' skin over the Activa RC. Once sent, the command reached the Activa RC with a latency of 105ms. This communication system is an investigational prototype restricted to research that is not approved for commercial use.

DECODING OF HOTSPOT INITIATION EVENTS FROM NEURAL SIGNALS

Concept

We sought to re-establish the natural dynamics of the spinal motor neuron activity by reinforcing the hotspots of motor neuron activity by stimulating the proprioceptive fibres of the spinal dorsal roots that feed into those motor neurons. Therefore, we aimed to deliver the stimulation protocols targeting appropriate roots beginning at the time that these hotspots become active. We hypothesized that leg motor cortical neuronal activity can enable accurate detection of these hotspot initiation events using the neural decoding approach. Therefore, we developed and implemented neural signal processing and decoding algorithms that served to detect initiation of hotspots from the neural activity. We implemented the algorithms within our real-time software application.

Acquisition of calibration data

To calibrate our decoders, we first collected a calibration dataset composed of synchronized neural signals and hotspot initiation events (**Extended Data Fig. 4a**). We acquired a dataset containing neural and video recordings of monkeys walking across a corridor without using stimulation. During the acquisition, the Central computer application (Blackrock Microsystems Inc., USA) band-pass filtered (0.5-7.5kHz) the wideband 96-channel neural signals recorded at 30 kilo-samples per second. Each crossing of this signal from above to below the electro-specific threshold was marked as a multiunit spike. The threshold was set to be 3.5 times the standard deviation of the filtered signal on this channel calculated over a period of five seconds. These multiunit spike events and the video recordings were saved on the computer. Once the dataset was recorded, we loaded the saved multiunit spikes into our custom-made Matlab program (The MathWorks, Inc., USA). We used the program to estimate multiunit spike rates using overlapping 150ms bins updated every 0.5 ms. We manually identified left and right foot off and foot strike gait events through visual inspection of the video frames. We synchronized the gait events with the multiunit spike rates using a trigger saved with the neural data that marked the onset of video recordings. Using the spatiotemporal map of motor neuron activity, we estimated the temporal shifts between foot off and foot strike gait events and the initiation of weight acceptance and leg lift hotspots. We used these shifts to co-register weight acceptance and leg lift hotspot initiation events with the multiunit spike rates. The hotspot events were additionally corrected for the empirically estimated stimulation latency of 105ms. We then used the corrected hotspot initiation events and the derived 96 channels multiunit spike rates to calibrate a regularized linear discriminant analysis decoder.

Decoder calibration

Through the process of decoder calibration, corrected hotspot initiation events served to identify sets of motor cortical multiunit spike features that correspond to those events. Specifically, sets of left and right weight acceptance and leg lift hotspot events, lwa, rwa, lll and rll, were used to derive the left and right weight acceptance and leg lift hotspot classes of neural features, C_{lwa}, C_{rwa}, C_{lll} and C_{rll}, respectively (**Extended Data Fig. 4a**):

$$C_{lwa}=\left\{\overline{a}_{lwa}\left|\overline{a}_{lwa}(i)=\begin{bmatrix}x_1\left(lwa(i)-\Delta t_{lwa}\right)\\ x_1\left(lwa(i)-\Delta t_{lwa}-\Delta t\right)\\ \vdots\\ x_1\left(lwa(i)-\Delta t_{lwa}-\left(N_{TP}-1\right)\cdot\Delta t\right)\\ x_2\left(lwa(i)-\Delta t_{lwa}\right)\\ \vdots\\ x_{N_{CH}}\left(lwa(i)-\Delta t_{lwa}-\left(N_{TP}-1\right)\cdot\Delta t\right)\end{bmatrix}\right.\right\}\quad C_{rwa}=\left\{\overline{a}_{rwa}\left|\overline{a}_{rwa}(i)=\begin{bmatrix}x_1\left(rwa(i)-\Delta t_{rwa}\right)\\ x_1\left(rwa(i)-\Delta t_{rwa}-\Delta t\right)\\ \vdots\\ x_1\left(rwa(i)-\Delta t_{rwa}-\left(N_{TP}-1\right)\cdot\Delta t\right)\\ x_2\left(rwa(i)-\Delta t_{rwa}\right)\\ \vdots\\ x_{N_{CH}}\left(rwa(i)-\Delta t_{rwa}-\left(N_{TP}-1\right)\cdot\Delta t\right)\end{bmatrix}\right.\right\}$$

$$C_{lll}=\left\{\overline{a}_{lll}\left|\overline{a}_{lll}(i)=\begin{bmatrix}x_1\left(lll(i)-\Delta t_{lll}\right)\\ x_1\left(lll(i)-\Delta t_{lll}-\Delta t\right)\\ \vdots\\ x_1\left(lll(i)-\Delta t_{lll}-\left(N_{TP}-1\right)\cdot\Delta t\right)\\ x_2\left(lll(i)-\Delta t_{lll}\right)\\ \vdots\\ x_{N_{CH}}\left(lll(i)-\Delta t_{lll}-\left(N_{TP}-1\right)\cdot\Delta t\right)\end{bmatrix}\right.\right\}\quad C_{rll}=\left\{\overline{a}_{rll}\left|\overline{a}_{rll}(i)=\begin{bmatrix}x_1\left(rll(i)-\Delta t_{rll}\right)\\ x_1\left(rll(i)-\Delta t_{rll}-\Delta t\right)\\ \vdots\\ x_1\left(rll(i)-\Delta t_{rll}-\left(N_{TP}-1\right)\cdot\Delta t\right)\\ x_2\left(rll(i)-\Delta t_{rll}\right)\\ \vdots\\ x_{N_{CH}}\left(rll(i)-\Delta t_{rll}-\left(N_{TP}-1\right)\cdot\Delta t\right)\end{bmatrix}\right.\right\}$$

where $\overline{a}_{lwa}$, $\overline{a}_{rwa}$, $\overline{a}_{lll}$ and $\overline{a}_{rll}$ are feature vector members of classes C_{lwa}, C_{rwa}, C_{lll} and C_{rll}, respectively; N_{TP}=7 (monkeys M8 and M9) or 5 (monkeys M10 and M11) is the number of multiunit spike rate measurements taken from the same neural channel; Δt = 50ms (M9), 67ms (M8), 75ms (M10) or 125ms (M11) is the temporal difference between the two consecutive spike rate measurements taken from the same neural channel; N_{CH} = 49 (M8), 64 (M9) or 96 (M10 and M11) is the number of neural channels; and Δt_{lwa}, Δt_{rwa}, Δt_{lll} and Δt_{rll} are the temporal offsets for each of the hotspots (for derivation of offsets, see section "Calculation of temporal offsets"). Another class C_{OTHER} representing states other than hotspot initiation events was formed:

$$C_{OTHER}=\left\{\overline{a}_O\left|\overline{a}_O(i)=\begin{bmatrix}x_1\left(t_i\right)\\ x_1\left(t_i-\Delta t\right)\\ \vdots\\ x_1\left(t_i-\left(N_{TP}-1\right)\cdot\Delta t\right)\\ x_2\left(t_i\right)\\ \vdots\\ x_{N_{CH}}\left(t_i-\left(N_{TP}-1\right)\cdot\Delta t\right)\end{bmatrix}\right.,\begin{array}{ll}t_i<lwa-\Delta t_{lwa}-10ms & \\ t_i>lwa-\Delta t_{lwa}+10ms & \\ t_i<rwa-\Delta t_{rwa}-10ms & \forall lwa\\ t_i>rwa-\Delta t_{rwa}+10ms & \forall rwa\\ t_i<lll-\Delta t_{lll}-10ms & ,\forall lll\\ t_i>lll-\Delta t_{lll}+10ms & \forall rll\\ t_i<rll-\Delta t_{rll}-10ms & \\ t_i>rll-\Delta t_{rll}+10ms & \end{array}\right\}$$

where t_i are all times at least 10ms away from all *lwa*, *rwa*, *lll* and *rll* events. To limit the computational complexity of the decoder calibration and, therefore, limit the time needed to calibrate the decoder, we selected up to 100 000 t_i–s by making random draws from a uniform distribution without repetitions. If less than 100 000 t_i–s were available, all t_i–s were used for calibration. C_{lwa}, C_{rwa}, C_{lll}, C_{rll} and C_{OTHER} were used to calibrate a multiclass regularized linear discriminant analysis (rLDA)[2,4] decoding model. We used

previously described procedures to implement the regularization[2,5,6], using a regularization parameter value of 0.4.

Calculation of temporal offsets

We sought to deliver the stimulation protocols that reinforced the hotspots of spinal motor neuron activity throughout the times at which the monkeys attempted to initiate movements that correspond to those hotspots. We hypothesized that these times can be decoded by thresholding the probability of observing motor cortical neuronal activity that corresponds to hotspot initiation events at 0.8. However, the motor state probabilities often crossed the probability threshold before the motor state actually occurred, which was closer to the probability maximum.

To account for all of these latencies, we derived offsets specific to each hotspot initiation event, Δt_{lwa}, Δt_{rwa}, Δt_{lll} and Δt_{rll}. as follows. First, we calibrated the decoder with all offsets set to 0ms. We then calculated the probability of every feature vector $F(t)$ in the calibration dataset to belong to one of C_{lwa}, C_{rwa}, C_{lll} and C_{rll} classes using the decoder. When one of these hotspot event probabilities crossed a threshold of 0.8, that hotspot event was detected – marked as e_{lwa}, e_{rwa}, e_{lll} and e_{rll}, respectively. On detection, the same hotspot event could not be detected as the next event for the following one second. We then calculated the median difference between the decoded and corrected hotspot initiation events, $\Delta\hat{t}_{lwa}$, $\Delta\hat{t}_{rwa}$, $\Delta\hat{t}_{lll}$ and $\Delta\hat{t}_{rll}$.

$$\Delta\hat{t}_{lwa} = M\left(lwa - e_{lwa}\right) \qquad \Delta\hat{t}_{rwa} = M\left(rwa - e_{rwa}\right) \qquad \Delta\hat{t}_{lll} = M\left(lll - e_{lll}\right) \qquad \Delta\hat{t}_{rll} = M\left(rll - e_{rll}\right)$$

where M is the median operator. Only the closest estimated event to the gait event of the same type was taken into account. We used the median value to exclude type I and type II errors from affecting the estimate of the offsets. We then added $\Delta\hat{t}_{lwa}$, $\Delta\hat{t}_{rwa}$, $\Delta\hat{t}_{lll}$ and $\Delta\hat{t}_{rll}$ to Δt_{lwa}, Δt_{rwa}, Δt_{lll} and Δt_{rll}, respectively, and calibrated the decoder with the new temporal offsets. We repeated this procedure until each of $\Delta\hat{t}_{lwa}$, $\Delta\hat{t}_{rwa}$, $\Delta\hat{t}_{lll}$ and $\Delta\hat{t}_{rll}$ were between -5ms and 5ms.

Calibration of decoders robust to the influence of stimulation on the neuronal activity

Once calibrated, the decoder was loaded into our real-time data processing and decoding software application running on the control computer. We could then apply our brain-controlled spinal cord neuroprosthesis – neuroprosthetic system that triggered spinal stimulation on detection of hotspot initiation events from neural activity – to monkeys M8-M11. However, the spinal cord stimulation affected the motor cortical neuronal activity, thereby deteriorating the accuracy of brain-controlled spinal stimulation. To improve the robustness of our decoder to the effects of stimulation, we adapted the previously developed two-step decoder calibration technique[2]. This technique uses the “first-step” decoder calibrated using the data recorded without the use of stimulation to generate the dataset where neural data is affected with the accurately delivered stimulation. Our goal was to synchronize the delivery of six stimulation protocols, each designed to reinforce one of left and right weight acceptance, propulsion and leg lift motor neuron activity hotspots. When delivered accurately, at least one of the stimulation protocols would be in effect throughout the majority of the gait cycle (see **Extended Data Fig. 5a** for example). Therefore, as the monkeys walk using the brain-controlled spinal cord neuroprosthesis to trigger all stimulation protocols, neuronal activity throughout the whole gait cycle will be affected by the stimulation. This would deteriorate the decoding accuracy and, in turn, desynchronize the delivery of the stimulation from the hotspots of motor neuron

activity leading to suboptimal efficacy of the brain-controlled spinal cord neuroprosthesis (**Extended Data Fig. 6**). Our strategy to overcome this problem was to trigger composite sequences of stimulation protocols that occupy only half of the gait cycle using hotspot initiation events that occur only once in a gait cycle. Since gait cycles exceeded 1s, and we used less than 0.5s of neuronal data history to detect the hotspot events, we reasoned that the neuronal signals corresponding to that hotspot event would not be substantially affected by the stimulation response.

We first acquired a corridor dataset without spinal stimulation and used it to calibrate the "first step" decoder as described above. We then acquired two additional corridor dataset in which the first step decoder sparsely triggered composite stimulation sequences. In the first dataset, the decoder used only the detection of left weight acceptance hotpot events to trigger left composite stimulation sequence composed of left weight acceptance, left propulsion and right leg lift stimulation protocols. The second dataset used only the detection of right weight hotspot events to trigger the right composite stimulation sequence composed of right weight acceptance, right propulsion and left leg lift stimulation protocols. The protocols in each composite sequence were arranged to overlap according to the spatiotemporal map of motor neuron activity. As the composite sequences lasted for less than half of the gait cycle, the sparse once-per-gait-cycle triggering prevented the stimulation from influencing the neural activity used to detect the hotspot events and, thereby, preserved accurate decoding (**Extended Data Fig. 4b**). These two datasets were combined with the original dataset recorded without stimulation and used altogether to calibrate the "second step" decoder. This decoder was then used to enable brain-control of the spinal cord neuroprosthesis. Since calibrated on neural activity both affected and unaffected by stimulation, the second step decoder maintained its accuracy in both presence and absence of stimulation (**Extended Data Fig. 4b**).

Temporal accuracy of the decoders

An ideal asynchronous neural decoder will use the neural activity to decode behavioral events that perfectly coincide with the actual behavioural events. However, due to variability of neural signals, finite sampling of calibration data and recording noise, behavioural events decoded even by a very accurate decoder will deviate in time from the actual events. Nonetheless, events decoded within an accepted tolerance window around the actual event are still useful for BCI applications. This acceptable tolerance will depend on the specific BCI application. Therefore, we measured the effectiveness of an asynchronous decoder by counting the proportion of actual gait events (left and right foot off and foot strike events) that had one and only one decoded event of the same type within the tolerance window of ± 200 ms.

Random delivery of EES protocols

Following the tuning and the testing of the brain-controlled spinal cord neuroprosthesis, we have performed a control that tested potential benefits of randomly delivered EES protocols as follows. We have first calibrated a decoder that inaccurately detected hotspot initiation events, but maintained a similar detection frequency. Monkeys then walked across the corridor as we used this inaccurate decoder to trigger delivery of the same EES protocols used for testing of the neuroprosthesis. We then identified trials that had the normalized mutual information between the actual and detected hotspot initiation events below 0.2 using a ±200 ms tolerance window[5]. These trials were classified as trials with random EES delivery.

MEDICAL IMAGING OF P1 STIMO-PARK PARTICIPANT

Structural MRI scan

P1 underwent a structural MRI scan of the thoracolumbar (T10-L5) spine on a 1.5 T system (Magnetom Sola, Siemens Healthineers) with 16-channel body and 32-channel spine array coils. Shimming was used to correct for magnetic field inhomogeneities. We acquired two 3D T2-weighted steady-state gradient-echo sequences with the following parameters: a) coronal True Fast Imaging with Steady state Precession (TrueFISP; Siemens Healthineers): repetition time (TR), 9.59 msec; echo time (TE), 4.80 msec; number of signal averages, 1; flip angle, 45 degrees; bandwidth, 566 Hz/pixel; field of view, 240 × 270 mm2; acquisition matrix, 384 × 216 pixels; section thickness, 0.6 mm; reconstructed voxel size, 0.6 × 0.6 × 0.6 mm3 b) sagittal Constructive Interference in Steady State (CISS, Siemens Healthineers): TR, 10.46 msec; TE, 5.23 msec; number of signal averages, 1; flip angle, 70 degrees; bandwidth, 211 Hz/pixel; field of view, 300 × 300 mm2; acquisition matrix, 320 × 320 pixels; section thickness, 0.9 mm; reconstructed voxel size, 0.9 × 0.9 × 0.9 mm3. The acquisition time was 17 min 10 sec and 7 min 09 sec for TrueFISP and CISS sequences, respectively.

CT scan of the torso

Computed tomography (CT) of the torso with the pelvis was performed on a 256-detector row CT system (Revolution Apex, GE Healthcare) using the following data acquisition parameters: tube potential, 120 kVp; tube current, 133-201 mA, by enabling automatic tube current modulation; gantry revolution time, 0.35 sec; beam collimation, 128 × 0.625 mm; pitch, 0.508. Images were reconstructed with a field of view of ~175 × 175 and 350 × 350 mm2 for the spine and pelvis, respectively; at a section thickness/interval of 1.25/1.25 mm, with both smooth (Standard) and sharp (Bone plus) convolution kernels and a deep learning image reconstruction algorithm (TrueFidelity, GE Healthcare) for image noise reduction. The nominal voxel size was 0.34 × 0.34 × 1.25 and 0.68 × 0.68 × 1.25 mm3 for the spine and pelvis, respectively.

DATA PROCESSING AND ANALYSIS

Deriving spatiotemporal maps of motor neuron activity in NHPs

We constructed spatiotemporal maps of motor neuron activity by projecting muscle activity into the spinal segments according to spatial distribution of motor pools. Contributions of each muscle were combined to compute the total activity at each spinal segment. The motor output pattern of each spinal segment S_i was estimated by the following equation:

$$S_i = \frac{\sum_{j=1}^{n_i} MN_{ij} EMG_j}{\sum_{j=1}^{n_i} MN_{ij}}$$

where EMG_j represents the normalized electromyography envelope of j-th muscle, n_i is the number of EMG_j-s corresponding to the i-th segment, and MN_{ij} is the number of motor neurons of j-th muscle in the i-th segment. We used the previously constructed library of distributions of the motor neurons across the lumbar spinal cord segments of different muscles[2,7] to derive MN_{ij}-s. Maps of motor neuron activity during the experimental sessions were computed using electromyography envelopes normalized to their 95th percentile over the whole session. Maps of motor neuron activity during single-pulse stimulation were

derived from the peak-to-peak electromyography response and normalized by the maximal response for each muscle.

Deriving spatiotemporal spinal maps of motor neuron activity in human

We used the same approach ad in NHPs, considering left and right hip flexors (Il, RF), knee extensors (VLat, RF), ankle flexors (TA) and ankle extensors (MG). We generated separate left and right spatiotemporal spinal maps based on activity of muscles on that side. We approximated $MN_{i,j}$ the by ratio of motoneurons innervating the muscle *j* and present in the spinal segment *i*, with respect to all motoneurons innervating the muscle *j*, as derived from electrophysiological measures in a large population of patients undergoing surgery[8] (**Supplementary Table 9**).

Calculation of gait parameters in NHPs

Before the recording sessions, we painted the anatomical landmarks of monkeys' legs using reflective paint. We recorded the videos of monkeys as they walked across corridor or ladder during the sessions using a 4-6 camera SIMI system (SIMI Motion Gmbh, Germany). After the session, we used the SIMI Motion software to reconstruct the 3D positions of each of the painted joints. We rotated the derived kinematics to align the x-axis with the forward movement of the monkey along the course; and to align x-y plane with the corridor or ladder surface. We used a custom-developed Matlab program to identify the foot off and foot strike events of both legs through visual inspection of the frames. We then used a custom Matlab program to calculate 83 gait parameters from each step by combining the derived 3D kinematics and the identified gait events (see **Supplementary Table 3** for the list of gait parameters). Steps were defined as movement starting and ending with a foot strike event. Gait parameters of left and right steps were merged in a single dataset.

Analysis of gait kinematics using principal component analysis (PCA) in NHPs

Execution of locomotor tasks involves the repetition of stereotypical patterns of leg movements. However, legs move with numerous degrees of freedom, which makes the characterization of gait difficult. In contrast, efficacy of a given therapy aiming to improve leg movements can be faithfully illustrated only by using a small number of meaningful parameters that consolidate the full complexity of locomotor patterns. Here, we computed 83 variables that quantified kinematic features of locomotor patterns (**Supplementary Table 3**). We assigned these variables to groups according to their relationship to the locomotor patterns. The groups include Gait cycle timing, Step dimensions, Endpoint velocity, Balance, Forward-Backward oscillations, Joint angles, Oscillatory amplitude, Oscillatory speed, Coordination and Reproducibility. To consolidate our dataset into a small number of parameters relevant to PD, we used principal component analysis (PCA) – a linear transformation of the dataset into a coordinate system where each new added axis maximizes the variance. Our dataset was arranged in a matrix with 83 variables as the matrix columns and each row representing one gait cycle (one observation). Data collected from different conditions and different monkeys (where applicable) were pooled together in a single matrix and z-scored across columns. Two or three principal components were typically sufficient to account for more than 50% of the total variance of observations, demonstrating the high correlation between therapy-induced changes of sets of variables. To visualize the differences between conditions and monkeys (where applicable), we illustrated the gait cycles of all the conditions and monkeys in the new space created by the first two or three principal components by plotting "balloons" – ellipsoids with the center and principal semi-axis as the mean and standard deviation calculated across all the gait cycles for that condition and monkey. In this representation,

the distance increases with the difference between the underlying locomotor patterns, allowing us to readily visualize differences of locomotor patterns between conditions. We also used PCA to identify the sets of variables that vary together to account for the differences between conditions. This is done using the factor loadings – the correlation between each variable and each principal component axis. The result of this analysis is displayed using a color-coded representation of correlation values of all the variables with up to three leading principal components (**Extended Data Fig. 1b-c,** and **Extended Data Fig. 7a**). In this representation, variables that together strongly correlate (either positively or negatively) with a given principal component form variable sets that account for a specific difference between conditions.

Calculation of crossing time in NHPs

We quantified the aggregate capacity of a monkey to walk as the time monkeys took to cross the central portion of the corridor or ladder. To this end, we first cooregistered the coordinate system across recordings performed on different days to a single coordinate system. The origin of this system was in the same place on the corridor or a ladder with the y axis in the middle direction is along the middle line of the corridor/ladder. We achieved this by marking 4 screws in the left top edge and right top edge of the corridor or ladder cage, respectively. We then linearly regressed left edge screws $S_{li}(x_{li}, y_{li}, z_{li})$ in the XY plane:

$$a_l x_{li} + b_l = y_{li}\ , i = 1,2,3,4$$

We used the least squares method to obtain:

$$\begin{bmatrix} a_l \\ b_l \end{bmatrix} = (A^T A)^{-1} A^T B$$

Where

$$A = \begin{bmatrix} x_{l1} & 1 \\ x_{l2} & 1 \\ x_{l3} & 1 \\ x_{l4} & 1 \end{bmatrix}, B = \begin{bmatrix} y_{l1} \\ y_{l2} \\ y_{l3} \\ y_{l4} \end{bmatrix}$$

The direction vector of the fitted line is:

$$\overrightarrow{d_l} = (1, a_l)$$

The rough direction vector of left edge in XY plane is:

$$\overrightarrow{r_l} = (x_{l4} - x_{l1}, y_{l4} - y_{l1})$$

We then obtained the unit direction vector of left edge:

$$\overrightarrow{n_l} = sgn(\overrightarrow{d_l} \cdot \overrightarrow{r_l}) \cdot \frac{\overrightarrow{d_l}}{|\overrightarrow{d_l}|}$$

Using the same procedure, we obtained the unit direction vector of right edge $\overrightarrow{n_r}$. We defined the y-axis unit vector as the bisector of two edges:

$$\overrightarrow{n_y} = \frac{\overrightarrow{n_l} + \overrightarrow{n_r}}{|\overrightarrow{n_l} + \overrightarrow{n_r}|} = (x_n, y_n)$$

Therefore, the unit vectors of the standard coordinate system are:

$$\hat{\imath}' = \begin{bmatrix} y_n \\ -x_n \\ 0 \end{bmatrix}, \hat{\jmath}' = \begin{bmatrix} x_n \\ y_n \\ 0 \end{bmatrix}, \hat{k}' = \begin{bmatrix} 0 \\ 0 \\ 1 \end{bmatrix}$$

We then calculated the rotation matrix from the coordinate system used to record the kinematics to the standard coordinate system as:

$$RM = inv \begin{bmatrix} y_n & -x_n & 0 \\ x_n & y_n & 0 \\ 0 & 0 & 1 \end{bmatrix}$$

To synchronize the origin of coordinate system, we calculated the center of these four screws in the X-Y plane:

$$c_x = \frac{1}{8} \sum_{i=1}^{4} (x_{li} + x_{ri})$$

$$c_y = \frac{1}{8} \sum_{i=1}^{4} (y_{li} + y_{ri})$$

The translation matrix is then:

$$TM = [-c_x \quad -c_y \quad 0]$$

Thus, the full transformation from the coordinate system used to record the kinematics to the standard coordinate system is:

$$(x' \quad y' \quad z') = (x \quad y \quad z) \cdot RM + TM$$

We then marked the position of the left crest joint at the start and end points of steady walking in each corridor or ladder crossing, and transformed them in the standard coordinate system. We used this points to identify the furthest point in the corridor/ladder where the monkey starts the steady walk, and the closest point where the monkey stops to walk steadily. Clear outliers were removed from this analysis. The space between these two points along the y-axis, common closest and furthest points of steady walk, defined the central portion of the corridor/ladder.

We then used the full left crest joint kinematics transformed into the standard coordinate system to find times when the monkey crossed into this central portion. We defined the time monkeys spent in this central portion during one crossing as the crossing time. We calculated the steady speed as the length of the central portion along the y axis divided by the crossing time.

Reconstruction of body posture in NHPs

We employed a whole-body CT scan to generate a 3D model of the rhesus macaque skeleton and biomechanics. We first created a control rig (Maya, Autodesk Inc., USA) comprised of 34 bones that accurately modelled whole-body posture. This skeleton allowed us to animate and reproduce the behavior of the monkeys in 3D. We then mapped the skeleton onto the whole-body kinematics recorded during behavioral experiments, and we rendered the corresponding mesh to obtain a high-fidelity replica of body posture at specific times of gait. We computed the spinal curvature from this model using the coordinates of twelve points in the sagittal plane distributed along the spine of the modelled skeleton. For each triplet

of points <*a,b,c*>, we computed the radius of the circumscribed circle that passes through these points according to:

$$R = \left\| \frac{a^2 \cdot \big((b-a) \times (c-a)\big) \times (b-a)}{\big\|\big((b-a) \times (c-a)\big)\big\|} \right\|$$

For the 12 points along the spine, this gave 10 values representing local curvature. We summarized the total spine curvature by taking the root-mean-square value of these calculations.

SUPPLEMENTARY TABLES

Animal ID	Macaque species	Walking experiments before MPTP	Walking experiments after MPTP	Wireless muscle activity system	Micro electrode array	Spike sorting	Spinal implant	Single pulse spinal cord stimulation	Brain-control stimulation before MPTP	Brain-control stimulation after MPTP
M1	Mulata	✓	✓	-	-	-	-	-	-	-
M2	Mulata	✓	✓	-	-	-	-	-	-	-
M3	Mulata	✓	✓	-	-	-	-	-	-	-
M4	Mulata	✓	✓	-	-	-	-	-	-	-
M5	Mulata	✓	✓	✓	✓	-	-	-	-	-
M6	Mulata	✓	✓	✓	✓	✓	-	-	-	-
M7	Mulata	✓	✓	✓	✓	✓	-	-	-	-
M8	Mulata	✓	✓	✓	✓	-	✓,&	✓	✓	✓
M9	Fascicularis	✓	✓	✓	✓	-	✓,&	✓	-	✓
M10	Mulata	-	-	✓	✓	-	✓,&	✓	✓	*
M11	Mulata	-	-	*	✓	-	✓,º	*	-	✓

✓ Performed
- Not performed
* Could not be performed due to technical issues or health conditions
& Commercial spinal implant
º *e-dura* spinal implant

Supplementary Table 1. Experimental procedures conducted on the NHPs.

Monkey	Session	PD score	# of blocks Stimulation Off	# of blocks Brain Control: LFS	# of blocks Brain Control: RFS	# of blocks Brain Control: LFS+RFS	# of blocks Brain Control: Both	# of blocks Brain control: Both - anticipated	# of blocks Brain control: Both - delayed	# of blocks Continuous stimulation	# of blocks DBS	# of blocks Brain control with DBS
M1	Pre-MPTP 1: corridor 19.7.2012	N/A	5									
	Post-MPTP 1: corridor 22.11.2012	7 (assessed on 22.11.2012)	5									
M2	Pre-MPTP 1: corridor 13.7.2012	N/A	6									
	Post-MPTP 1: corridor 22.11.2012	9 (assessed on 22.11.2012)	4									
M3	Pre-MPTP 1: corridor 26.2.2013	N/A	5									
	Pre-MPTP 2: corridor 27.2.2013	N/A	5									
	Pre-MPTP 3: ladder 9.5.2013	N/A	5									
	Post-MPTP 1: corridor 17.10.2013	6 (assessed on 17.10.2013)	4									
	Post-MPTP 1: ladder 17.10.2013	6 (assessed on 17.10.2013)	8									
	Post-MPTP 2: corridor 25.11.2013	7 (assessed on 25.11.2013)	5									
M4	Pre-MPTP 1: corridor 9.4.2013	N/A	9									
	Pre-MPTP 1: ladder 9.4.2013	N/A	12									

	Post-MPTP 1: ladder 2.6.2013	5 (assessed on 2.6.2013)	6
	Post-MPTP 2: corridor 3.12.2013	6 (assessed on 3.12.2013)	5
M5	Pre-MPTP 1: corridor 23.11.2013	N/A	12
	Pre-MPTP 1: ladder 23.11.2013	N/A	8
	Pre-MPTP 1: treadmill 23.11.2013	N/A	7
	Pre-MPTP 2: corridor 24.11.2013	N/A	10
	Pre-MPTP 2: ladder 24.11.2013	N/A	9
	Pre-MPTP 2: treadmill 24.11.2013	N/A	7
	Post-MPTP 1: treadmill 19.12.2013	0 (assessed on 19.12.2013)	1
	Post-MPTP 2: treadmill 26.12.2013	0 (assessed on 26.12.2013)	1
	Post-MPTP 3: treadmill 9.1.2014	2 (assessed on 9.1.2014)	6
	Post-MPTP 4: treadmill 16.1.2014	2 (assessed on 16.1.2014)	5
	Post-MPTP 5: treadmill 23.1.2014	6 (assessed on 16.1.2014)	1
	Post-MPTP 6: treadmill 13.2.2014	5 (assessed on 13.2.2014)	1
	Post-MPTP 7: treadmill 21.4.2014	6 (assessed on 21.4.2014)	5

	Post-MPTP 8: corridor 23.4.2014	6 (assessed on 23.4.2014)	10
	Post-MPTP 8: ladder 23.4.2014	6 (assessed on 23.4.2014)	11
	Post-MPTP 8: treadmill 23.4.2014	6 (assessed on 23.4.2014)	4
	Post-MPTP 9: corridor 28.4.2014	5 (assessed on 28.4.2014)	6
	Post-MPTP 10: treadmill 5.6.2014	4 (assessed on 5.6.2014)	3
	Post-MPTP 11: treadmill 6.6.2014	4 (assessed on 6.6.2014)	3
	Post-MPTP 12: treadmill 7.6.2014	4 (assessed on 7.6.2014)	7
	Post-MPTP 13: treadmill 24.7.2014	4 (assessed on 26.7.2014)	2
	Post-MPTP 14: treadmill 25.7.2014	4 (assessed on 26.7.2014)	5
	Post-MPTP 15: treadmill 26.7.2014	4 (assessed on 26.7.2014)	4
	Post-MPTP 16: treadmill 28.7.2014	4 (assessed on 28.7.2014)	5
	Post-MPTP 17: treadmill 29.7.2014	4 (assessed on 29.7.2014)	3
	Post-MPTP 18: treadmill 30.7.2014	4 (assessed on 30.7.2014)	3

M6	Pre-MPTP 1: treadmill 22.11.2013	N/A	1
	Pre-MPTP 2: corridor 24.11.2013	N/A	10
	Pre-MPTP 2: ladder 24.11.2013	N/A	6
	Pre-MPTP 2: treadmill 24.11.2013	N/A	1
	Pre-MPTP 3: corridor 26.11.2013	N/A	11
	Pre-MPTP 3: ladder 26.11.2013	N/A	10
	Pre-MPTP 3: treadmill 26.11.2013	N/A	1
	Post-MPTP 1: treadmill 19.12.2013	0 (assessed on 19.12.2013)	1
	Post-MPTP 2: treadmill 26.12.2013	0 (assessed on 26.12.2013)	1
	Post-MPTP 3: treadmill 2.1.2014	2 (assessed on 02.01.2014)	3
	Post-MPTP 4: treadmill 9.1.2014	7 (assessed on 09.01.2014)	2
	Post-MPTP 5: treadmill 16.1.2014	7 (assessed on 16.01.2014)	2
	Post-MPTP 6: treadmill 23.1.2014	6 (assessed on 23.01.2014)	3
	Post-MPTP 7: treadmill 30.1.2014	5 (assessed on 30.01.2014)	1
	Post-MPTP 8: treadmill 6.2.2014	5 (assessed on 06.02.2014)	3

	Post-MPTP 9: treadmill 13.2.2014	7 (assessed on 13.02.2014)	3
	Post-MPTP 10: treadmill 18.2.2014	7 (assessed on 18.02.2014)	4
	Post-MPTP 11: corridor 22.2.2014	7 (assessed on 22.02.2014)	4
	Post-MPTP 11: treadmill 22.2.2014	7 (assessed on 22.02.2014)	8
	Post-MPTP 12: corridor 25.2.2014	7 (assessed on 25.02.2014)	6
	Post-MPTP 12: treadmill 25.2.2014	7 (assessed on 25.02.2014)	4
	Post-MPTP 13: treadmill 27.2.2014	7 (assessed on 27.02.2014)	3
	Post-MPTP 14: corridor 7.4.2014	6 (assessed on 07.04.2014)	15
	Post-MPTP 14: treadmill 7.4.2014	6 (assessed on 07.04.2014)	1
	Post-MPTP 15: corridor 10.4.2014	6 (assessed on 10.04.2014)	9
	Post-MPTP 15: treadmill 10.4.2014	6 (assessed on 10.04.2014)	2
	Post-MPTP 16: corridor 16.4.2014	6 (assessed on 16.04.2014)	15

	Post-MPTP 16: treadmill 16.4.2014	6 (assessed on 16.04.2014)	1
	Post-MPTP 17: treadmill 18.4.2014	6 (assessed on 16.04.2014)	2
	Post-MPTP 18: corridor 5.5.2014	5 (assessed on 05.05.2014)	13
	Post-MPTP 18: ladder 5.5.2014	5 (assessed on 05.05.2014)	12
	Post-MPTP 18: treadmill 5.5.2014	5 (assessed on 05.05.2014)	1
	Post-MPTP 19: treadmill 6.5.2014	6 (assessed on 06.05.2014)	2
	Post-MPTP 19: treadmill 8.5.2014	5 (assessed on 08.05.2014)	1
	Post-MPTP 20: corridor 9.5.2014	5 (assessed on 09.05.2014)	15
	Post-MPTP 20: ladder 9.5.2014	5 (assessed on 09.05.2014)	15
	Post-MPTP 21: treadmill 9.5.2014	5 (assessed on 09.05.2014)	1
	Post-MPTP 22: corridor 4.6.2014	5 (assessed on 04.06.2014)	4
	Post-MPTP 23: treadmill 5.6.2014	5 (assessed on 05.06.2014)	2

	Post-MPTP 24: treadmill 6.6.2014	5 (assessed on 06.06.2014)	8
	Post-MPTP 25: treadmill 7.6.2014	5 (assessed on 07.06.2014)	4
	Post-MPTP 26: treadmill 24.7.2014	5 (assessed on 26.07.2014)	11
	Post-MPTP 27: treadmill 25.7.2014	5 (assessed on 26.07.2014)	8
	Post-MPTP 28: treadmill 26.7.2014	5 (assessed on 26.07.2014)	5
	Post-MPTP 29: treadmill 28.7.2014	5 (assessed on 28.07.2014)	8
	Post-MPTP 30: treadmill 29.7.2014	5 (assessed on 29.07.2014)	6
	Post-MPTP 31: treadmill 30.7.2014	5 (assessed on 30.07.2014)	5
M7	Pre-MPTP 1: corridor 2.12.2013	N/A	11
	Pre-MPTP 1: ladder 2.12.2013	N/A	11
	Pre-MPTP 1: treadmill 2.12.2013	N/A	8
	Pre-MPTP 2: corridor 4.12.2013	N/A	15
	Pre-MPTP 2: ladder 4.12.2013	N/A	5

	Pre-MPTP 2: treadmill 4.12.2013	N/A	1
	Pre-MPTP 3: corridor 5.12.2013	N/A	12
	Pre-MPTP 3: treadmill 5.12.2013	N/A	4
	Pre-MPTP 4: corridor 12.12.2013	N/A	11
	Pre-MPTP 4: treadmill 12.12.2013	N/A	8
	Pre-MPTP 5: corridor 13.12.2013	N/A	10
	Pre-MPTP 5: treadmill 13.12.2013	N/A	1
	Post-MPTP 1: treadmill 19.12.2013	0 (assessed on 19.12.2013)	7
	Post-MPTP 2: treadmill 26.12.2013	0 (assessed on 26.12.2013)	1
	Post-MPTP 3: treadmill 2.1.2014	3 (assessed on 02.01.2014)	2
	Post-MPTP 4: treadmill 27.1.2014	6 (assessed on 27.01.2014)	1
	Post-MPTP 5: treadmill 6.2.2014	6 (assessed on 06.02.2014)	2
	Post-MPTP 6: treadmill 13.2.2014	6 (assessed on 13.02.2014)	2
	Post-MPTP 7: treadmill 19.2.2014	6 (assessed on 19.02.2014)	6
	Post-MPTP 8: corridor 20.2.2014	6 (assessed on 20.02.2014)	10
	Post-MPTP 8: ladder 20.2.2014	6 (assessed on 20.02.2014)	13

	Post-MPTP 9: treadmill 21.2.2014	6 (assessed on 21.02.2014)	1			
	Post-MPTP 10: corridor 24.2.2014	6 (assessed on 24.02.2014)	12			
	Post-MPTP 10: treadmill 24.2.2014	6 (assessed on 24.02.2014)	2			
	Post-MPTP 11: ladder 26.2.2014	6 (assessed on 26.02.2014)	12			
	Post-MPTP 12: corridor 28.2.2014	6 (assessed on 26.02.2014)	12			
	Post-MPTP 12: treadmill 28.2.2014	6 (assessed on 26.02.2014)	1			
M8	Pre-MPTP 1: ladder 24.10.2017	N/A	9			
	Pre-MPTP 2: treadmill 25.10.2017	N/A	20			
	Pre-MPTP 3: corridor 30.11.2017	N/A	12			
	Pre-MPTP 4: treadmill 30.11.2017	N/A	4			
	Pre-MPTP 5: corridor 02.12.2017	N/A	24			
	Pre-MPTP 6: corridor 05.12.2017	N/A	8	3 at 40Hz 1 at 50 Hz	3 at 40Hz 2 at 50 Hz 2 at 60 Hz	
	Pre-MPTP 7: corridor 07.12.2017	N/A	10	8 at 40Hz	9 at 40Hz	5 at 30Hz 6 at 40Hz 1 at 50Hz

	Pre-MPTP 8: corridor 13.12.2017	N/A	12				
	Post-MPTP 1: treadmill 15.1.2018	10 (assessed on 13.01.2018)	4				
	Post-MPTP 1: corridor 15.1.2018	10 (assessed on 13.01.2018)	10				
	Post-MPTP 2: treadmill 27.1.2018	10 (assessed on 27.01.2018)	6				
	Post-MPTP 2: corridor 27.1.2018	10 (assessed on 27.01.2018)	4				
	Post-MPTP 3: treadmill 29.1.2018	10 (assessed on 27.01.2018)	13				
	Post-MPTP 4: treadmill 30.1.2018	10 (assessed on 27.01.2018)	10				
	Post-MPTP 4: corridor 30.1.2018	10 (assessed on 27.01.2018)	14				
	Post-MPTP 5: corridor 31.1.2018	10 (assessed on 03.02.2018)	20				
	Post-MPTP 6: corridor 2.2.2018	10 (assessed on 03.02.2018)	16	8 at 40Hz 9 at 50 Hz 6 at 60 Hz			7 at 250Hz 6 at 500 Hz
	Post-MPTP 6: ladder 2.2.2018	10 (assessed on 03.02.2018)	4	8 at 50 Hz 10 at 60 Hz			
	Post-MPTP 7: corridor 3.2.2018	10 (assessed on 03.02.2018)	7	6 at 40Hz 10 at 50 Hz 7 at 60 Hz	5 at 50Hz	5 at 50Hz	
	Post-MPTP 7: ladder 3.2.2018	10 (assessed on 03.02.2018)	7	8 at 50 Hz 4 at 60 Hz			
M9	Pre-MPTP 1: corridor 28.11.2018	N/A	14				
	Pre-MPTP 2: corridor 02.01.2019	N/A	11				

	Post-MPTP 1: corridor 21.2.2019	10 (assessed on 14.02.2019)	19							12 at 20Hz 17 at 125Hz	
	Post-MPTP 2: corridor 23.2.2019	10 (assessed on 14.02.2019)	10			11 at 80 Hz					
	Post-MPTP 3: corridor 25.2.2019	10 (assessed on 14.02.2019)									22 at DBS 125Hz and Brain control at 80Hz
	Post-MPTP 4: corridor 28.2.2019	10 (assessed on 12.03.2019)	6			6 at 40 Hz 5 at 60 Hz 5 at 80 Hz	6 at 80Hz	5 at 80Hz	6 at 250Hz 5 at 500Hz		
M10	Pre-MPTP 1: corridor 12.12.2017	N/A	5	1 at 30Hz 3 at 40Hz 1 at 50 Hz 1 at 60 Hz	1 at 30Hz 1 at 40Hz 3 at 50 Hz 1 at 60 Hz	4 at 30Hz 2 at 40Hz					
M11	Post-MPTP 1: corridor 27.2.2017	5 (assessed on 27.02.2017)	9			3 at 30Hz 8 at 40Hz 4 at 50 Hz 7 at 60 Hz 6 at 80 Hz					
	Post-MPTP 1: ladder 27.2.2017	5 (assessed on 27.02.2017)	6			6 at 60 Hz 10 at 80 Hz					
	Post-MPTP 2: corridor 28.2.2017	5 (assessed on 27.02.2017)	11			10 at 80 Hz					

Supplementary Table 2. Behavioral experiments conducted with each NHP.

PARAMETER	VARIABLE
Gait cycle timing	
1	Limb side (right or left)
2	Duration of gait cycle in seconds
3	Speed of animal
4	Stance duration in seconds (time between gait cycle onset and stance end)
5	Swing duration in seconds (time between stance end and gait cycle end)
6	Stance phase portion of the gait cycle (in percentage of gait cycle)
7	Time at stance / time of swing onset
Step dimensions	
8	Stride length
9	Step length
10	Path length of ankle marker (distance travelled by ankle marker from swing start to the end of the gait cycle)
11	Maximum backward position (crest - ankle positions)
12	Maximum forward position of the hip
13	Max limb length
14	Step height
15	Normalized step height
Endpoint velocity	
16	Maximal speed of Foot across the entire gait cycle
17	Gait cycle phase of the maximal speed of Foot
18	Acceleration of Foot at swing onset
19	Speed of Foot at swing onset
20	Angular velocity of Foot at swing onset
Balance	
21	Lateral displacement across the swing phase
22	Normalized maximal position of hip marker on Y axis
23	Normalized minimal position of hip marker on Y axis
24	Difference between normalized max and min positions of hip marker on Y axis
Forward-Backward oscillations	
25	Min of Crest-Hip elevation angle
26	Min of Hip-Knee elevation angle
27	Min of Knee-Ankle elevation angle
28	Min of Ankle-Foot elevation angle
29	Min of limb axis (Crest-Foot vector) angle in XY plane
30	Max of Crest-Hip elevation angle
31	Max of Hip-Knee elevation angle
32	Max of Knee-Ankle elevation angle
33	Max of Ankle-Foot elevation angle
34	Max of limb axis (Crest-Foot vector) angle in XY plane
Joint angles	
35	Max of Crest-Hip-Knee angle
36	Max of Hip-Knee-Ankle angle
37	Max of Knee-Ankle-Foot angle
38	Max of lateral limb axis (Crest-Foot vector) angle in YZ plane
39	Min of Crest-Hip-Knee angle

40	Min of Hip-Knee-Ankle angle
41	Min of Knee-Ankle-Foot angle
42	Min of lateral limb axis (Crest-Foot vector) angle in YZ plane
Oscillatory amplitude	
43	Difference between max and min of Crest-Hip elevation angle
44	Difference between max and min of Hip-Knee elevation angle
45	Difference between max and min of Knee-Ankle elevation angle
46	Difference between max and min of Ankle-Foot elevation angle
47	Difference between max and min of Crest-Foot elevation angle
48	Difference between max and min of Crest-Hip-Knee angle
49	Difference between max and min of Hip-Knee-Ankle angle
50	Difference between max and min of Knee-Ankle-Foot angle
51	Difference between max and min of the lateral limb axis (Crest-Foot vector) angle in YZ plane
Oscillatory speed	
52	Min of limb axis (Crest-Foot vector) angle velocity in XY plane
53	Min of Hip angle velocity
54	Min of Knee angle velocity
55	Min of Ankle angle velocity
56	Max of limb axis (Crest-Foot vector) angle velocity in XY plane
57	Max of Hip angle velocity
58	Max of Knee angle velocity
59	Max of Ankle angle velocity
60	Difference between max and min values of limb axis (Crest-Foot vector) angle velocity in XY plane
61	Difference between max and min values of Hip angle velocity
62	Difference between max and min values of Knee angle velocity
63	Difference between max and min values of Ankle angle velocity
Coordination	
64	Phase difference between two elevation angles: Hip-Knee minus Crest-Hip
65	Phase difference between two elevation angles: Knee-Ankle minus Hip-Knee
66	Phase difference between two elevation angles: Ankle-Foot minus Knee-Ankle
67	Gait cycle phase difference between min Crest-Hip elevation angle and min Hip-Knee elevation angle
68	Gait cycle phase difference between max Crest-Hip elevation angle and max Hip-Knee elevation angle
69	Gait cycle phase difference between min Hip-Knee elevation angle and min Knee-Ankle elevation angle
70	Gait cycle phase difference between max Hip-Knee elevation angle and max Knee-Ankle elevation angle
71	Gait cycle phase difference between min Knee-Ankle elevation angle and min Ankle-Foot elevation angle
72	Gait cycle phase difference between max Knee-Ankle elevation angle and max Ankle-Foot elevation angle
Reproducibility	
73	PC1 variance resulting from PCA applied on leg elevation angles
74	PC2 variance resulting from PCA applied on leg elevation angles
75	PC3 variance resulting from PCA applied on leg elevation angles
76	Phase of Crest-Hip elevation angle at maximal amplitude
77	Maximal amplitude of Crest-Hip elevation angle
78	Phase of Hip-Knee elevation angle at maximal amplitude
79	Maximal amplitude of Hip-Knee elevation angle
80	Phase of Knee-Ankle elevation angle at maximal amplitude
81	Maximal amplitude of Knee-Ankle elevation angle
82	Phase of Ankle-Foot elevation angle at maximal amplitude
83	Maximal amplitude of Ankle-Foot elevation angle

Supplementary Table 3 | Computed gait parameters from kinematic recordings.

ID	Sex	Age	Item 10	Item 11	Item 13	Total
C_002	F	60	0	0	0	0
C_004	M	54	0	0	0	0
C_005	M	68	0	0	1	1
C_006	M	58	0	0	0	0
C_007	M	53	0	0	0	0
C_008	F	59	0	0	1	1
C_009	F	62	0	0	1	1
C_010	F	56	0	0	1	1
C_011	M	60	0	0	0	0
PD_002	M	54	1	0	0	1
PD_003	F	72	0	0	1	1
PD_007	F	64	1	0	2	3
PD_008	F	67	1	3	2	6
PD_009	F	59	1	0	2	3
PD_010	F	49	0	0	1	1
PD_013	F	65	1	0	2	3
PD_014	M	67	1	0	1	2
PD_016	F	62	1	0	1	2
PD_017	F	66	2	0	1	3
PD_018	M	54	1	0	1	2
PD_019	M	39	2	0	1	3
PD_020	M	64	1	0	1	2
PD_021	M	55	2	0	1	3
PD_022	F	65	1	0	1	2
PD_023	F	65	1	0	1	2
PD_024	M	47	2	0	1	3
PD_025	F	68	1	0	1	2
PD_026	M	61	1	0	2	3
PD_027	M	67	0	0	2	2
PD_028	M	58	2	0	2	4
PD_029	M	67	2	3	2	7
PD_031	M	59	1	0	1	2
PD_032	F	54	1	0	1	2
PD_041	M	49	1	0	1	2

Supplementary Table 4 | MDS UPDRS III gait-related sub-scores for all individuals (healthy controls and PD) included in the cohort for characterizing gait deficits in Parkinson's disease.

PARAMETER	VARIABLE
Gait cycle timing	
1	Limb side (right or left)
2	Duration of gait cycle in seconds
3	Step duration
4	Stance duration in seconds (time between gait cycle onset and stance end)
5	Swing duration in seconds (time between stance end and gait cycle end)
6	Single stance phase portion of the gait cycle (in percentage of gait cycle)
7	Double stance phase portion of the gait cycle (in percentage of gait cycle)
Step dimensions	
8	Stride length
9	Step length
10	Step width
11	Stride speed
12	Path length of ankle marker (distance travelled by ankle marker from swing start to the end of the gait cycle)
13	Path length of toe marker
14	Step height
15	Max limb length
16	Amplitude of lateral movement of the hip
17	Amplitude of vertical movement of the hip
Oscillatory oscillations	
18	Min of hip-knee joint angle
19	Max of hip-knee joint angle
20	Difference between max and min of hip-knee elevation angle
21	Max of knee-ankle joint angle
22	Max of knee-ankle joint angle
23	Difference between max and min of knee-ankle elevation angle
24	Min of ankle-foot angle
25	Max of ankle-foot angle
26	Difference between max and min of ankle-foot angle
27	Min of leg elevation angle
28	Max of leg elevation angle
29	Difference between max and min of leg elevation angle
Oscillatory speed	
30	Max of hip angle velocity
31	Max of knee angle velocity
32	Max of ankle angle velocity
33	Max of limb axis (crest-foot vector) angle velocity in XY plane
Reproducibility	
34	Path length in 3 main PD components
35	Path width in 3 main PD components
36	Planarity in 3 main PD components
37	Phase of hip elevation angle at maximal amplitude
38	Phase of knee elevation angle at maximal amplitude
39	Phase of foot elevation angle at maximal amplitude

Supplementary Table 5 | Computed gait parameters from kinematic recordings in humans

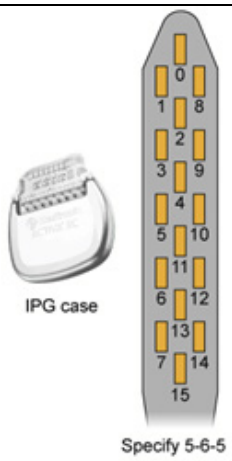

Protocol	Cathode	Anode	Current	Pulsewidth	Frequency
Left knee extension	5	3	0.6mA	300µs	60Hz
Left knee extension boost	5	3	0.7mA	300µs	60Hz
Left ankle extension	15	7	0.4mA	300µs	60Hz
Left hip flexion	1	0	1.4mA	300µs	60Hz
Left ankle flexion	7	IPG case	0.5mA	200µs	60Hz
Right knee extension	10	9	0.9mA	300µs	60Hz
Right knee extension boost	10	9	1mA	300µs	60Hz
Right ankle extension	14	12	0.5mA	300µs	60Hz
Right hip flexion	8	IPG case	1.7mA	300µs	60Hz
Right ankle flexion	12	14	0.6mA	200µs	60Hz

Supplementary Table 6 | Parametrization of EES protocols used to generate EES sequences.
Left. The panel shows the schematic of the IPG and the Specify 5-6-5 arrays with electrode numbers when looking at the array from the above. **Right.** Each protocol is characterized by its cathode, anode, current, pulsewidth and frequency. The EES parameters are provided for each of the ten different EES protocols used to generate EES sequences.

Sequence	Protocol	0 – 0.3s	0.3-0.7s	0.7-1.4s
Left Foot Off	Left knee extension			
	Left knee extension boost			
	Right knee extension boost			
	Right ankle extension			
	Left hip flexion			
	Left knee flexion			
Right Foot Off	Right knee extension			
	Right knee extension boost			
	Left knee extension boost			
	Left ankle extension			
	Right hip flexion			
	Right knee flexion			

Supplementary Table 7 | Characterization of Left Foot Off and Right Foot Off EES sequences.
Each EES sequence is 1.4s long and composed out of ten EES protocols defined in **Supplementary Table 6**, each promoting one of four left (red) or right (green) muscle synergies. The three rightmost columns show the temporal evolution of each sequence across three phases: 0s – 0.3s, 0.3s – 0.7s and 0.7s – 1.4s.

Item / Score	5	4	3	2	1	0
Safety	Safe			Supervision, risk of fall	Close supervision, high risk of fall	Assistance required to avoid fall
Fluidity	Good	Reduced	Absent			
Consistency across gait cycles	Good	Reduced	Absent			
Symmetry	Symmetric	Asymmetric				
Stepping thread	Normal heel to toe sequence	Abnormal				
Upper limb mobility	Good	Reduced				
Freezing, festination	Absent	Present				
Leg crossing	Absent	Present				

Supplementary Table 8 | Criteria used to determine the physiotherapist scores.

Spinal segment	Iliopsoas	Rectus Femoris and Vastus Lateralis	Tibialis Anterior	Medial Gastrocnemius
L1	0.45	0.12	0	0
L2	0.3	0.27	0	0
L3	0.17	0.37	0.04	0.04
L4	0.06	0.24	0.34	0.34
L5	0.01	0	0.43	0.43
S1	0.01	0	0.19	0.19
S2	0	0	0	0

Supplementary Table 9 | Coefficients to transfer EMG activity of muscles into activity of spinal segments.

	Month 0 (study start)				Month 6 (study end)			
	Medication DBS^{ON} - EES^{OFF}	Medication DBS^{ON} - EES^{ON}	Medication DBS^{OFF} - EES^{ON}	No medication, DBS^{OFF} - EES^{OFF}	Medication DBS^{ON} - EES^{OFF}	Medication DBS^{ON} - EES^{ON}	Medication DBS^{OFF} - EES^{ON}	No medication DBS^{OFF} - EES^{OFF}
10. Gait	2	2	2	4	1	0	3	Not tested
11. Freezing of gait	3	1	2	3	1	0	3	Not tested
12. Posture stability	0	0	0	3	0	0	3	Not tested
13. Posture	2	2	1	1	0	0	1	Not tested
14. Global spontaneity of movement	1	1	3	4	2	1	4	Not tested
TOTAL	**8**	**6**	**8**	**15**	**4**	**1**	**14**	**Not tested**

Supplementary Table 10 | MDS UPDRS III gait-related sub-scores of P1, measured after the neuroprosthesis implantation and at the end of the clinical trial protocol.

REFERENCES SUPPLEMENTARY INFORMATION

1. Capogrosso, M.*, et al.* Configuration of electrical spinal cord stimulation through real-time processing of gait kinematics. *Nature Protocols* **13**, 2031-2061 (2018).
2. Capogrosso, M.*, et al.* A brain–spine interface alleviating gait deficits after spinal cord injury in primates. *Nature* **539**, 284-288 (2016).
3. Minev, I.R.*, et al.* Biomaterials. Electronic dura mater for long-term multimodal neural interfaces. *Science* **347**, 159-163 (2015).
4. Friedman, J. Regularized Discriminant-Analysis. *J Am Stat Assoc*, 165-175 (1989).
5. Milekovic, T., Ball, T., Schulze-Bonhage, A., Aertsen, A. & Mehring, C. Detection of error related neuronal responses recorded by electrocorticography in humans during continuous movements. *PLoS One* **8**, e55235 (2013).
6. Milekovic, T.*, et al.* Stable long-term BCI-enabled communication in ALS and locked-in syndrome using LFP signals. *J Neurophysiol* **120**, 343-360 (2018).
7. Capogrosso, M.*, et al.* Configuration of electrical spinal cord stimulation through real-time processing of gait kinematics. *Nat Protoc* (2018).
8. Schirmer, C.M.*, et al.* Heuristic map of myotomal innervation in humans using direct intraoperative nerve root stimulation. *J Neurosurg-Spine* **15**, 64-70 (2011).